HTD-Vol. 364-3, Proceedings of the ASME
Heat Transfer Division — 1999
Volume 3
ASME 1999

3-D SINTERING OF TWO-COMPONENT METAL POWDERS WITH STATIONARY AND MOVING LASER BEAMS

Yuwen Zhang, A. Faghri, C.W. Buckley and T.L. Bergman
Department of Mechanical Engineering
University of Connecticut
Storrs, CT 06269-3139

Abstract

Melting and resolidification of a mixture of two metal powders with significantly different melting points under irradiation of a stationary or a moving Gaussian laser beam were investigated numerically and experimentally. The liquid motion driven by capillary and gravity forces as well as the shrinkage of the powder bed caused by the overall density change were taken into account in the physical model. The liquid flow was formulated by using Darcy's law, and the energy equation was given using a temperature transforming model. Predictions were compared with experimental results obtained with nickel braze and AISI 1018 steel powder. The effects of laser properties and the scanning velocity on the laser sintering process were also investigated. An empirical correlation that can be used to predict the of cross sectional area of the heat affected zone is proposed.

NOMENCLATURE

a	major axis length of the ellipsoid laser beam (m)
A	dimensionless major axis length of the ellipsoid laser beam, a/R
A_c	dimensionless cross section area
Bi	Biot number, hR/k_H
Bo	Bond number, $\rho_\ell g R d_p/\gamma_m^0$
C	dimensionless heat capacity, C^0/C_H^0
C^0	heat capacity, ρc_p (J/m^3K)
c_p	specific heat $(J/kg\,^oC)$
d_p	diameter of the powder particle (m)
g	gravitational acceleration (m/s^2)
h	convective heat transfer coefficient (W/m^2K)
$h_{s\ell}$	latent heat of fusion (J/kg)
i,j,k	unit vector in x, y, z directions
k	thermal conductivity $(W/m\,^oC)$
K	permeability (m^2) or dimensionless thermal conductivity, k/k_H
$K_{r\ell}$	relative permeability
Ma	Marangoni number, $\gamma_m^0 d_p/(\alpha_H \mu)$
N_i	dimensionless moving laser beam intensity, $\alpha_a P/[\pi R A k_H (T_m^0 - T_i^0)]$
N_R	radiation number,$\varepsilon_e \sigma (T_m^0 - T_i^0)^3 R/k_H$
N_t	temperature ratio for radiation, $T_m^0/(T_m^0 - T_i^0)$
p	pressure (N/m^2)
P	laser power (W)
P_c	dimensionless capillary pressure, $p_c/[\gamma_m^0\sqrt{\epsilon/K}]$
R	radius of the laser beam or minor axis length of ellipsoid laser beam (m)
s	solid-liquid interface location (m)
s_0	location of surface (m)
s_{st}	sintered depth (m)

Sc	subcooling parameter, $C_H^0(T_m^0 - T_i^0)/(\rho_L h_{s\ell})$
T	dimensionless temperature, $(T^0 - T_m^0)/(T_m^0 - T_i^0)$
t	time (s)
T^0	temperature (^oC)
v	velocity vector, $u\mathbf{i} + v\mathbf{j} + w\mathbf{k}$ (m/s)
$\mathbf{V}$	dimensionless velocity vector, $\mathrm{v}R/\alpha_H$
$\forall$	Volume (m^3)
x, y, z	coordinate (m)
X, Y, Z	dimensionless coordinate, $(x, y, z)/R$

Greek letters

α	thermal diffusivity (m^2/s)
α_a	absorptivity
γ^0	surface tension, (N/m^2)
γ	dimensionless surface tension, γ^0/γ_m^0
γ_m^0	surface tension of low melting point metal at melting point, (N/m^2)
ΔT^0	one half of phase change temperature range (K)
ΔT	one half of dimensionless phase change temperature range
ϵ	porosity for unsintered powder, $(\forall_g + \forall_\ell)/(\forall_g + \forall_\ell + \forall_s + \forall_H)$
ϵ_e	emissivity of snrface
η_{st}	dimensionless sintered depth, s_{st}/R
μ	dynamic viscousity, (kg/ms)
ρ	density (kg/m^3)
σ	Stefan-Boltzmann constant, $5.67 \times 10^{-8}\ W/(m^2K^4)$
τ	dimensionless time, $\alpha_H t/R^2$
φ	volume fraction, $\forall/(\forall_s + \forall_\ell + \forall_H + \forall_g)$
$\dot{\Phi}_L$	dimensionless volume production rate
ψ	saturation, φ_ℓ/ϵ
∇	gradient operator, $\mathbf{i}\frac{\partial}{\partial x} + \mathbf{j}\frac{\partial}{\partial y} + \mathbf{k}\frac{\partial}{\partial z}$
$\hat{\nabla}$	dimensionless gradient operator, $\mathbf{i}\frac{\partial}{\partial X} + \mathbf{j}\frac{\partial}{\partial X} + \mathbf{k}\frac{\partial}{\partial Z}$

Subscripts

c	capillary
g	gas(es)
H	high melting point powder
i	initial
ℓ	liquid or sintered region
L	low melting point powder
m	melting point
s	solid particle of the low melting point powder
v	vapor

INTRODUCTION

Selective Laser Sintering (SLS) is an emerging technology of Solid Freeform Fabrication (SFF) in which 3-D parts can be built from CAD data (Beaman et al., 1997). The material used in SLS includes amorphous (e.g. polycarbonate), semi-crystalline (e.g. nylon), and crystalline (e.g. metal) powder. The thermal models that are available in the literature are primarily concerned with sintering of amorphous powders (Sun and Beaman, 1995; Williams et al., 1996; Kandis and Bergman, 1997; Beaman et al., 1997). Since amorphous powder has little crystallinity and a near zero latent heat of fusion, no phase change occnrs during sintering. Some researchers simply establish the thermal model associated with sintering of an amorphous powder as a pure conduction problem (Sun and Beaman, 1995; Williams et al., 1996). Kandis and Bergman (1997) present an experimental investigation and a numerical prediction of the sintering of polymer powder in a square annulus with external heating and internal cooling. Kandis et al. (1999) investigate sintering of a polymer powder bed under irradiation of a stationary laser beam. The effect of the powder particle motion due to shrinkage phenomena on the thermal phenomena is taken into account in Kandis and Bergman (1997) and Kandis et al. (1999).

SLS of metal powder involves fabrication of near full density objects from powder via melting induced by a directed laser beam (generally CO_2 or YAG) and resolidification. For sintering of metal powder, the latent heat of fusion is usually very large, and therefore melting and resolidification phenomena have a significant effect on the temperature distribution in the parts and powder, the residual stress in the part, local sintering rates, and the final quality of the parts. A significant change of density accompanies the melting process because the volume fraction of gas(es) in the powder decreases from a value as large as 0.6 to nearly zero after melting. In addition, the liquid metal infiltrates into the unsintered region due to capillary and gravity forces.

Bunnell (1995) and Manzur et al. (1996) propose the use of a powder mixture containing two powders with significantly different melting points, in which only the low melting point powder will be molten and resolidified during the SLS process. In

this process, the low melting point powder melts and infiltrates to the unsintered region due to capillary and gravity forces. The solid particles of the high melting point powder may also move downward because the high melting point powder cannot sustain the powder bed alone. It is very clear that both liquid and solid in the powder bed have their own velocities, and these velocities may have a significant effect on the energy transport in the powder bed.

The modeling of SLS of metal powder is a very challenging task. A thorough survey of the existing literature indicates that scant attention has been paid to thermal modeling of the sintering of metal powder. Shah (1994) experimentally investigated melting of a single column of solder particle (eutectic Sn-Pb) held vertically inside a glass tube. The problem is then formulated using an enthalpy model and solved using a finite difference method. Zhang and Faghri (1999) analytically solve a 1-D melting problem in a powder bed containing a powder mixture under a boundary condition of the second kind. The results show that the shrinkage effect on the melting of the powder bed is not negligible. Zhang and Faghri (1998) numerically investigate 2-D melting and resolidification of a two-component metal powder with a moving Gaussian heat source. The shrinkage phenomena induced by the overall density change is taken into account. However, the liquid flow driven by capillary and gravity force is neglected in Zhang and Faghri (1998). Pak and Plumb (1997) present a 1-D thermal model of melting of two-component powder bed. The liquid motion driven by capillary and gravity forces is considered, but the velocity of non-melting powder particle induced by shrinkage is ignored.

A 3-D thermal model of SLS of a metal powder bed that contaius a mixture of two powders with significantly different melting points will be presented in this paper. The liquid flow driven by capillary and gravity forces and the solid particle velocity induced by shrinkage of the powder bed will be taken into account. The predicted results are compared with experimental results obtained with nickel braze and AISI 1018 steel powder. The effect of the laser beam scanning velocity on the sintering process will be discussed.

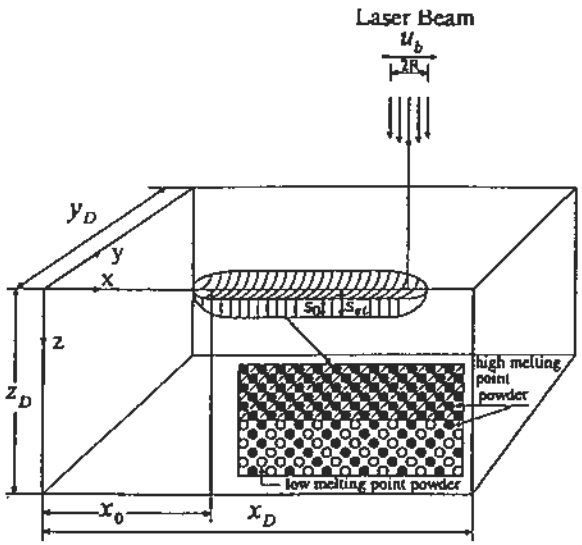

Figure 1: Physical model of the 3-D sintering of two-component metal powder

PHYSICAL MODEL

Problem statement

The physical model of the problem is shown in Fig. 1. A powder bed, which contains two powders with significantly different melting points, with a uniform initial temperature, T_i, below the melting point of the low melting point powder, T_m, is in a cavity with a size of $x_D \times 2y_D \times z_D$ (length $\times$ width $\times$ height). The coordinate system is also shown in Fig. 1. For the cases of an expanded stationary laser beam, the center of the elliptic Gaussian laser beam is located at the center of the top surface of the powder bed ($x = 0, y = 0$) with the major axis of ellipse aligned with x axis. For the cases of a moving laser beam, a round Gaussian laser beam scans the surface of the cavity starting form a point $x = x_0$ toward the positive direction of the x axis with a constant velocity, u_b. In practice, the temperature of the powder bed is not allowed to reach the melting point of the high melting point powder and therefore only the low melting point powder melts and resolidifies. As the laser beam interacts with the powder, the temperature of the powder increases to T_m which induces melting. The molten metal infiltrates the unsintered region of the powder bed due to the driving forces of capillarity and gravity. The infiltration of the

liquid metal affects the melting process, and from the practical point of view, it can be very helpful in producing fully densified parts (Bunnell, 1995). The top surface of the melted powder bed recedes since the low melting point material is molten and the high melting point material alone cannot sustain the powder bed. After the laser beam moves away, the liquid pool cools and resolidifies to form a densified heat affected zone (HAZ). These zones, formed by multiple laser scans, are subsequently interwoven to form a layer part.

For the melting of a powder bed that contains melting and non-melting powders, both a constant volume model (Mughal and Plumb, 1993) and a constant porosity model (Pak and Plumb, 1997) have been employed to predict the transient thermal response of the system. For the situation where the melting particles are significantly smaller than the non-melting particles, melting particles can occupy the interstitial space between the larger particles of non-melting material. The volume of the powder bed is unchanged after the low melting point particles change phase because the skeletal matrix formed by the non-melting particles is able to support the powder alone. For melting and non-melting powder particles with the sizes of same order of magnitude (which is the case for SLS of metal powder) the non-melting powder's skeletal structure collapses after the low melting point powder is liquidified. In this case, the conservation of mass principles can be used to show that the porosity of the powder bed remains constant (while the volume of the powder bed shrinks; Pak and Plumb, 1997). In addition to this constant porosity assumption, the following assumptions are made:

1. The thermal properties of both powders are independent of the temperature with exception of the surface tension of the low melting point liquid metal, which is treated as a linear function of temperature. The thermal properties of the low melting point powder are the same for both solid and liquid phases.

2. The contributions of the gas(es) to the density and heat capacity of the powder bed are negligible (Zhang and Faghri, 1998,1999).

3. The velocity of the solid induced by the shrinkage has only a component in the z direction ($\mathbf{v}_s = w_s\mathbf{k}$; Kandis et al., 1999). However, the liquid flow in all three directions is taken into account ($\mathbf{v}_\ell = u_\ell\mathbf{i} + v_\ell\mathbf{j} + w_\ell\mathbf{k}$).

4. The linear Darcy's law can be utilized to describe the liquid metal flow in the powder bed.

5. The pressure of the gas phase remains constant at one atmosphere.

Velocities and Volume Fractions

Since the system is symmetric about the (x, z) plane, only half of the cavity ($0 < y < y_D$) needs to be studied. The liquid velocities must satisfy the continuity equation:

$$\frac{\partial \varphi_\ell}{\partial t} + \nabla \cdot (\varphi_\ell \mathbf{v}_\ell) = \dot{\Phi}_L^0 \tag{1}$$

where $\dot{\Phi}_L^0$ is the volumetric production rate of the liqnid due to melting.

Likewise, the solid low melting point powder vanishes at the same rate, i.e.

$$\frac{\partial \varphi_s}{\partial t} + \frac{\partial (\varphi_s w_s)}{\partial z} = -\dot{\Phi}_L^0 \tag{2}$$

The high melting point powder particles have the same velocity as the particles of the low melting point powder particles. Therefore, the continuity equation for the high melting point material is

$$\frac{\partial \varphi_H}{\partial t} + \frac{\partial (\varphi_H w_s)}{\partial z} = 0 \tag{3}$$

The volume fractions of each species satisfies $\varepsilon + \varphi_s + \varphi_H = 1$, where the porosity of the powder bed, ε, is defined as the total volume of void, including the volumes of gas and liquid, relative to the total volume of the powder bed. Adding eqs. (2) and (3) and considering the volume fraction definition along with the constant porosity assumption, one can obtain:

$$\dot{\Phi}_L^0 = -(1 - \varepsilon)\frac{\partial w_s}{\partial z} \tag{4}$$

The volume production rate is zero in all the regions except at the solid-liquid interface where the phase change is taking place. The solid velocity is zero in the unsintered region. In the melted region, $\partial w_s / \partial z = 0$. Therefore, the solid velocity in the melted region is the same as the shrink velocity at the surface of the powder bed and can be

expressed as $w_s = \partial s_0/\partial t$, $s_0 < z < s$. The solid velocity can be determined by integrating eq. (3) and the result is (Zhang, 1998)

$$w_s = \begin{cases} 0 & z > s \\ \dfrac{\varphi_{si}}{1-\varepsilon}\dfrac{\partial s}{\partial t} & z < s \end{cases} \tag{5}$$

The liquid flow occurs in three directions, and the velocities can be determined using Darcy's law

$$\mathbf{v}_\ell - w_s\mathbf{k} = -\frac{KK_{r\ell}}{\varphi_\ell \mu}\left(\nabla p_\ell - \rho_\ell g\mathbf{k}\right) \tag{6}$$

where the permeability of the porous medium, K, can be determined by use of the Carman-Kozeny equation (Kaviany, 1995):

$$K = \frac{d_p^2 \varepsilon^3}{180(1-\epsilon)^2} \tag{7}$$

The relative permeability, $K_{r\ell}$, can be expressed as $K_{r\ell} = \psi_e^3$ (Pak and Plumb, 1997), where ψ_e is the normalized saturation:

$$\psi_e = \begin{cases} \dfrac{\psi - \psi_{ir}}{1-\psi_{ir}} & \psi > \psi_{ir} \\ 0 & \psi \le \psi_{ir} \end{cases} \tag{8}$$

Considering the constant gas phase pressure assumption, eq. (6) becomes

$$\mathbf{v}_\ell - w_s\mathbf{k} = \frac{KK_{r\ell}}{\varphi_\ell \mu}\left(\nabla p_c + \rho_\ell g\mathbf{k}\right) \tag{9}$$

The capillary pressure can be calculated using the Leverett function expressed as $p_c = a\left(\psi_e + b\right)^c \gamma^0 \sqrt{\varepsilon/K}$, where a, b, and c are empirical constants with values of 0.38, 0.014, and 0.27 respectively (Pak and Plumb, 1997). The surface tension of the low melting point liquid metal, γ^0, is expressed as a linear function of temperature, $\gamma^0 = \gamma_m^0\left[1 - \gamma^{0\prime}(T^0 - T_m^0)\right]$.

It can be seen that the liquid velocities are functions of the saturation, ψ, which is related to the liquid fraction, φ_ℓ, (i.e. $\varphi_\ell = \psi\varepsilon$; Pak and Plumb, 1997). On the other hand, the solution of φ_ℓ from eq. (1) requires the liquid velocities. Therefore, the liquid fraction and the liquid velocities must be obtained by solving eqs. (1) and (9) simultaneously.

Energy Equation

The temperature transforming model using a fixed grid method (Cao and Faghri, 1990) is employed to describe melting and resolidification in the powder bed. This model is based upon the assumption that the melting and solidification processes occur over a range of temperatures from $(T_m^0 - \Delta T^0)$ to $(T_m^0 + \Delta T^0)$, but it can also be used to simulate the melting and solidification processes occurring at a single temperature by using a very small value of ΔT^0. This model has the advantage of eliminating the time step and grid size limitations that are normally encountered in other fixed grid methods. In the fixed coordinate system, (x, y, z), the energy equation is

$$\begin{aligned} &\frac{\partial}{\partial t}\left\{\left[\varphi_H C_H^0 + (\varphi_\ell + \varphi_s)C_L^0\right]T^0\right\} \\ &+ \nabla\cdot\left(\varphi_\ell \mathbf{v}_\ell C_L^0 T^0\right) + \frac{\partial}{\partial z}\left[w_s(\varphi_H C_H^0 + \varphi_s C_L^0)T^0\right] \\ &= \nabla\cdot\left(k\nabla T^0\right) - \left\{\frac{\partial}{\partial t}\left[(\varphi_\ell + \varphi_s)S^0\right]\right. \\ &\left. + \nabla\cdot(\varphi_\ell \mathbf{v}_\ell S^0) + \frac{\partial}{\partial z}\left(\varphi_s w_s S^0\right)\right\} \end{aligned} \tag{10}$$

The heat capacity of the high melting point powder is

$$C_H^0 = \rho_H c_{pH} \tag{11}$$

The effective heat capacity of the low melting point metal can be expressed as

$$C_L^0(T^0) = \begin{cases} \rho_L c_{pL} & \left|T^0 - T_m^0\right| > \Delta T^0 \\ \rho_L c_{pL} + \dfrac{\rho_L h_{s\ell}}{2\Delta T^0} & \left|T^0 - T_m^0\right| \le \Delta T^0 \end{cases} \tag{12}$$

and S^0 in eq. (10) is defined as

$$S^0(T^0) = \begin{cases} 0 & T^0 - T_m^0 < -\Delta T^0 \\ \dfrac{\rho_L h_{s\ell}}{2} & \left|T^0 - T_m^0\right| \le \Delta T^0 \\ \rho_L h_{s\ell} & T^0 - T_m^0 > \Delta T^0 \end{cases} \tag{13}$$

The thermal conductivity of the powder bed is calculated by

$$k = \begin{cases} k_{eff} & T^0 - T_m^0 < \Delta T^0 \\ k_{eff} + \dfrac{k_\ell - k_{eff}}{2\Delta T^0}(T^0 - T_m^0 + \Delta T^0) & |T^0 - T_m^0| \le \Delta T^0 \\ k_\ell & T^0 - T_m^0 > \Delta T^0 \end{cases} \tag{14}$$

where, k_{eff} is the effective thermal conductivity of the unsintered powder bed. It can be calculated using the empirical correlation proposed by Hadley (1986). When the low melting point powder is molten, the contact area between the two materials is significantly increased, and therefore it is expected that the effective thermal conductivity of the mixture of low melting point liquid metal (or resolidified low melting point metal, in the sintered region) and high melting point powder is higher than that before melting. The thermal conductivity of a liquid or resolidified part is therefore calculated using

$$k_\ell = (\varphi_\ell + \varphi_s)\, k_L + \varphi_H k_H \tag{15}$$

In the arrival of eq. (15), it is assumed the thermal resistance of the powder and the gas(es) is a parallel arrangement, and the contribution of the thermal conductivity of the gas(es) is neglected since it is much smaller than that of both powders (Zhang and Faghri, 1998, 1999).

The difference between the liquid and sintered region is that the temperature of the latter is lower than T_m, and it exists in the form of solid. It is obvious that the low melting point material in the sintered region cannot flow because it exists in the solid state. For the convenience of programming, the volume fraction of the low melting point metal is still represented by φ_ℓ, and the summation of φ_ℓ and φ_g holds constant, ε, even in the sintered region. The viscosity of the low melting point metal in the sintered region can be set as a very large value so that a low melting point metal velocity of zero can be achieved (Cao and Faghri, 1990).

The boundary and initial conditions of the energy equation are

$$-k\frac{\partial T^0}{\partial z} = \frac{\alpha_a P}{\pi R^2 A}\exp\left[-\frac{(x - x_0 - u_b t)^2}{a^2} - \frac{y^2}{R^2}\right] - \varepsilon_e \sigma\left[T^{0\,4} - T_\infty^{0\,4}\right] - h(T^0 - T_\infty^0),\ z = s_0(x,y) \tag{16a}$$

$$\partial T^0/\partial z = 0, \qquad z = z_D \tag{16b}$$

$$\partial T^0/\partial x = 0, \qquad x = 0, \quad x_D \tag{16c}$$

$$\partial T^0/\partial y = 0, \qquad y = 0, \quad y_D \tag{16d}$$

$$T^0 = T_i^0, \qquad t = 0 \tag{17}$$

Dimensionless Governing Equations

In order to reduce the dependent variables and make the solution more general, the governing equations and the corresponding boundary conditions should be nondimensionalized. The dimensionless forms of the energy equation is obtained by nondimensionalizing eq. (11), i.e.

$$\frac{\partial (CT)}{\partial t} + \hat{\nabla}\cdot(\varphi_\ell \mathbf{V}_\ell C_L T) + \frac{\partial}{\partial Z}\left[W_s(\varphi_H + \varphi_s C_L)T\right] = \hat{\nabla}\cdot(K\,\hat{\nabla}\,T) - \left\{\frac{\partial}{\partial \tau}\left[(\varphi_\ell + \varphi_s)S\right] + \hat{\nabla}\cdot(\varphi_\ell \mathbf{V}_\ell S) + \frac{\partial}{\partial Z}(\varphi_s W_s S)\right\} \tag{18}$$

where the dimensionless velocities of the liquid phase, which are calculated by the dimensionless form of eq. (9)

$$\mathbf{V}_\ell - W_s \mathbf{k} = \frac{\varepsilon Ma \psi_e^3}{\sqrt{180}(1-\varepsilon)\psi}\,\hat{\nabla} P_c + \frac{\varepsilon^2 Ma Bo \psi_e^3}{180(1-\varepsilon)^2 \psi}\mathbf{k} \tag{19}$$

satisfy the nondimensional continuity equation of the liquid, which is obtained by nondimensionalizing eq. (1)

$$\frac{\partial \varphi_\ell}{\partial \tau} + \hat{\nabla}\cdot(\varphi_\ell \mathbf{V}_\ell) = \dot{\Phi}_L \tag{20}$$

The boundary condition of eq. (18) at the top surface of the powder bed is

$$-K\frac{\partial T}{\partial Z} = N_i \exp\left[-\frac{(X - X_0 - U_b\tau)^2}{A^2} - Y^2\right] - N_R\left[(T + N_t)^4 - (T_\infty + N_t)^4\right] - Bi(T - T_\infty),\quad Z = S_0(X,Y) \tag{21}$$

The nondimensional form of other equations can be obtained using dimensionless variables defined in the nomenclature (Zhang, 1998).

NUMERICAL SOLUTION

Equation (18) is a typical convection-diffusion equation which can be discretized by a finite volume method (Patankar, 1980) and solved numerically. The simulation of the entire problem requires solutions of: (1) the velocity and the volume fraction of the solid phase of the low and high melting point powder particles; (2) the velocities and the volume fraction of melted low melting point metal, and (3) the temperature distribution and the location of solid-liquid interface, and the sintering interface. The solutions of the above three subproblems are conjugated and an iteration is needed. The outline of the solution procedure can be found in Zhang (1998). The powder bed (which includes unsintered powder, a liquid pool, and sintered region) has an irregular shape since the upper surface of the powder bed recedes due to shrinkage that occurs in the sintering process. The computational region expansion approach (Patankar, 1980) is employed in this paper to deal with the irregular geometric shape.

Since eqs. (18) and (20) are non-linear, iterations are needed. During the iteration process, some underrelaxation is necessary. The relaxation factor used here is $0.1 \sim 0.2$. In order to simulate the melting and resolidification process occurring at a single temperature, a very small dimensionless phase-change temperature range, $\Delta T = 0.01$, is used in the calculation. The grid number used in the numerical simulation was $72 \times 37 \times 37$ (in the x, y, and z directions) for stationary scanning cases and $168 \times 37 \times 37$ for moving laser beam scanning cases. The dimensionless time step for the cases with both stationary and moving laser beam was $\Delta\tau = 0.05 \sim 0.1$ when the laser is on and $\Delta\tau = 0.5$ after the laser is shut off. A finer grid ($112 \times 52 \times 52$ for stationary laser beam and $202 \times 82 \times 82$ for moving laser beam) and a smaller time step ($\Delta\tau = 0.01$) were also used to simulate some cases, but the difference in the predicted values of the dimensionless cross section area was less than 0.5%.

EXPERIMENTAL APPARATUS AND PROCEDURE

It is important to note that successful fabrication of metal parts requires a careful match between the surface properties of the two materials. Specifically, the liquid phase low melting point material must wet the non-melting solid particles in order to (1) fabricate full density parts and (2) apply the model developed here. Identification of powder pairs with these characteristics is not trivial (Bunnell, 1995) and hence specific materials are used here. Unfortunately, the thermophysical properties of the powders are not well-documented and, as will become evident, some properties must be estimated in order to predict the experimental results.

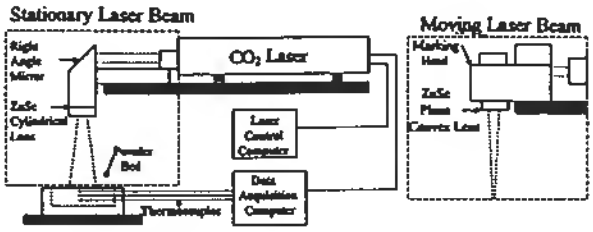

(a) Stationary laser beam system (b) Marking head for moving laser beam system

Figure 2: Experimental apparatus for sintering of metal powder

Table 1 Size of the powder particles

	nickel braze	AISI 1018
Average diameter	45 μm	68 μm
Minimum diameter	20 μm	61 μm
Maxmum diameter	93 μm	74 μm
STD	15 μm	4.4 μm

Experiments were conducted using a mixture of 40% nickel braze powder and 60% AISI 1018 carbon steel powder by volume. The shapes of both powder particles are spherical and the size distributions of both powder particles are listed in Table 1. The experimental apparatus is shown in Fig. 2. Two types of experiments were conducted: one using a stationary line source and the other using a traversing circular beam. During the tests, the powder was contained in a block of Plexiglas with a pocket machined into it with dimensions 76.2× 76.2×19 mm (length×width×height), with the surface of the powder exposed to the atmosphere. Prior to laser irradiation, the powder surface was leveled with a straight edge to obtain a smooth, flat surface. The initial porosity of the powder was determined to be 0.4 by a simple mass/volume measurement procedure.

To measure the transient temperature within the powder, Teflon coated, 0.076-mm diameter, chromel-alumel (K type) thermocouples were strung across the test pocket at three different depths (2.1, 4.3, 6.5 mm $\pm$ 0.25 mm), with the thermocouple leads aligned parallel to the surface. A Pentium-based PC, with Keithley Metrabyte A/D and thermocouple boards, was used to acquire and log three-thermocouple readings and a voltage signal from the laser control computer. The laser signal was acquired at 20 Hz, and used to define the time the laser was turned on and off, to within $\pm$ 0.05 seconds. The thermocouple readings were acquired at 7 Hz, with an estimated uncertainty of $\pm 1.1^0 C$.

The irradiation was provided by a CW, 50 W (maximum), CO_2 laser (Synrad 48-5) operating at 10.6-mm wavelength with a Gaussian intensity distribution. The actual laser power was measured using an Oriel model 70266 (S/N 30362) laser power meter, positioned between the ZnSe lens and the powder surface. For the stationary line source tests, a right angle first surface mirror and a 50.8-mm focal length, anti reflection coated ZnSe cylindrical lens was used to transform the round Gaussian beam into an ellipsoid Gaussian beam. The size of the ellipsoid laser beam can be adjusted by changing the separation distance between the lens and surface of the powder bed.

During the traversing circular beam experiments, the first surface mirror and cylindrical lens were replaced by a laser beam positioning device (Synrad, SH series Marking Head, model number SH3-370CH / 180), equipped with a 508 mm focal length plano-convex ZnSe lens. Two different traversing speeds (1.32 mm/s and 2.65 mm/s) were used. In both cases, the laser power was held at 31 watts and the scan length was maintained at 20 mm. The radius of the Gaussian beam measured at $1/e^2$ is 2 mm (or 1.41 mm at $1/e$).

For both stationary and traversing experiments, the solid heat affected zone formed by laser irradiation was extracted and mounted in Bakelite. The mounted specimens were sectioned in the desired location and polished for examination. Cross sections were photographed using a Nikon Metaphot reflected light microscope with a spatial resolution of 0.5 μm.

RESULTS AND DISCUSSION

Radiative coupling between the laser radiation and the powder is a crucial effect to consider in the modeling since it determines the amount of laser energy delivered to the material. The value of absorptivity is usually very low for most metals at room temperature, but increases with an increase of the target material temperature (Von Allmen, 1986). Alternatively, the absorptivity of liquid metal is not a strong function of temperature, and it is comparable to that of solid metals near their melting points (Siegel and Howell, 1992). The effective absorptivity of the powder bed is expected to be much higher than that of bulk metal since the portion of the laser irradiation entering the pore space of a powder bed is trapped due to multiple reflections (Sun and Beaman, 1995). The absorptivity of nickel braze bulk material is estimated by to be that of Inconel (Touloukian, 1967) because the two materials's components are similar. Likewise, the absorptivity of the high melting point powder material, AISI 1018 steel, can be estimated from Brandes (1983). After a careful comparison and a trial and error procedure, the absorptivity of the powder bed is taken to be 0.5; a value which provided predictions which best agreed with the experimental results.

Table 2. The sintering parameters applied in the numerical calculation.

Bi	2.94×10^{-4}	Sc	1.38
Bo	5.30×10^{-3}	T_∞	-1.0
C_L	1.07	X_D	53.88
K_g	5.38×10^{-4}	Y_D	26.94
K_L	0.20	Z_D	13.47
Ma	1042.0	ϵ	0.40
N_R	1.19×10^{-3}	φ_{si}	0.24
N_T	1.31	ψ_{ir}	0.08

Thermal properties of the AISI 1018 steel are not directly available in the literature. Therefore, properties of AISI 1010 (Incropera and DeWitt, 1996) were used. The density and the melting point of nickel braze are available from the manufacturer (Wall Colmonoy Corporation, 1997). Values for thermal conductivity of nickel braze can be obtained from Touloukian (1967) while the specific heat of nickel braze was taken to be the weighted average of the specific heats of individual components (which are available from Brandes, 1983). The latent heat of melting can be

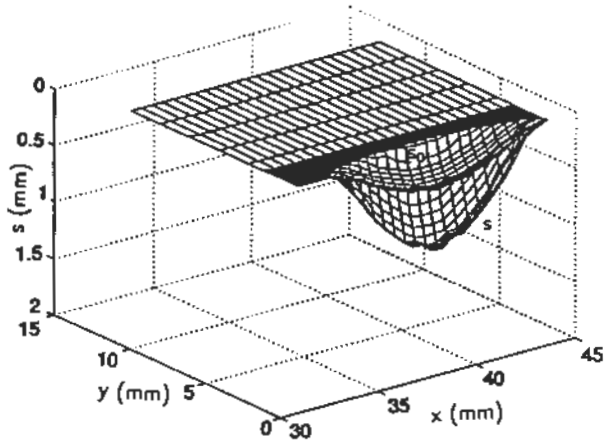

Figure 3: Shape of the HAZ with a stationary laser beam ($A = 3.95$, $N_i = 0.0223, U_b = 0$)

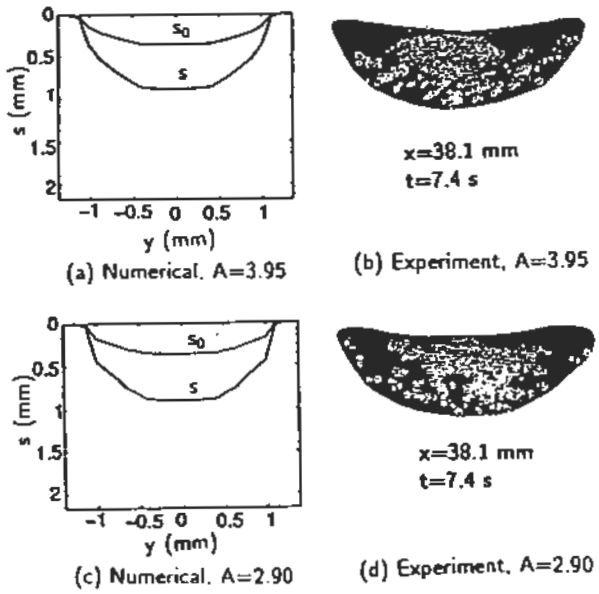

Figure 4: Comparison of the cross section area obtained by numerical simulation and experiment (stationary laser beam)

derived from the latent heats and melting points of the individual components (Brandes, 1983) and the result is $h_{s\ell} = 3.774 \times 10^5 J/kg$. Viscosity and surface tension for the liquid nickel braze are $\mu = 5.474 \times 10^{-3} kg/sm$ and $\gamma = 1.207 - 1.802 \times 10^{-4}(T - 1271) N/m$, which were obtained from semi-empirical equations in Iida and Guthrie (1988), Bunnell (1995), and Brandes (1983). Finally, the irreducible saturation, ψ_{ir}, was taken to be 0.08 (Kaviany, 1995). The dimensionless parameters that are used in the numerical simulation are listed in Table 2.

Numerical simulations were performed under conditions corresponding as closely as possible to those of the experiments. Numerical results were obtained in dimensionless form and were subsequently converted to dimensional form in order to compare with the corresponding experimental results. Fig. 3 shows the 3-D shape of the powder bed surface and HAZ after irradiation of a stationary ellipsoid laser beam using a power of $36.5W$ and a processing time of 7.4 s. The minor axis of the ellipsoid laser beam (defined as the radius where the intensity of the beam is 1/e of the centerline intensity) is 1.4 mm. The ratio of the major axis over minor axis of the ellipsoid laser beam, A, is 3.95. It can be seen that the top depression of the HAZ is ellipsoid, which corresponds to the shape of the laser beam. Thicknesses of the sintered HAZ (in the z direction) are greatest at the center of the beam and decrease with increasing x and y.

In order to view the shape clearly, the cross section of the HAZ at $x = 38.1\ mm$ is plotted in Fig. 4(a). A micrograph of the cross section at $x = 38.1\ mm$ is shown in Fig. 4(b) for comparison. The black area in the micrograph is a local void and the light area is sintered metal. The shape of HAZ, averaged locally in the x direction, corresponds to the outer boundaries of the dark region. It can be seen that the actual and predicted shapes of the HAZ are similar, but the local boundaries of the sintered and unsintered areas are somewhat different. The boundary between the sintered and unsintered regions is smooth and clear for the numerical result but it is not clear for the experimental result. A large degree of local porosity is evident in the actual piece. The mophological differences between the predictions and experimental results may suggest that there is a mushy zone between the sintered and unsintered region because the low melting point liquid metal and the solid particles may not be in thermal equilibrium in such a rapid process. Another possibility is that the continuum medium assumption may not be very good because the diameter of the laser beam is only two order of magnitude greater than the particle diameter. Further efforts will be needed to reveal the cause

of the non-smooth boundary between sintered and unsintered regions.

Fig. 4 (c) and (d) show the numerical and experimental HAZ cross sections for different operational conditions ($P = 28.5W, A = 2.9, t_s = 7.4s$). Basically, the characteristics of the numerical and experimental results are similar to those at the higher laser power and longer major axis of the laser beam. Since the laser intensity at the center of the laser beam is nearly the same, the differences in the cross sectional area are not significant for these two cases. The temperature histories at three different depths at $x = y = 0$ for the preceding two cases are shown in Fig. 5(a) and (b). It can be seen that the agreement between numerical and experimental results is excellent.

The SLS with a moving laser beam was investigated since it corresponds to the real process. Fig. 6(a) shows the predicted shape of the sintered region in three different cross sections. The laser beam starts to scan the powder bed from $x = 28.1$ mm and beam irradiation is curtailed at $x = 48.1$ mm. It can be seen that the shape and size of the cross sections at the three different x are similar. This suggests that the quasi-steady state has been achieved when the laser beam travels to $x = 34.1$ mm. Fig. 6(b) shows three cross sections corresponding to the numerical results in Fig. 6(a). It can be seen that the shapes of the numerical results agree fairly well with the experimental results. As can be seen from Fig. 6(b), some voids can be observed in the cross section of the sintered part. Again, this phenomenon was not observed in the numerical results because the porosity of the powder bed was assumed to remain constant in the process. However, the predicted and measured total volume of powder sintered in the process is very close.

In order to investigate the effect of the laser beam traversing velocity, numerical simulations and experiments were performed for a fast scanning velocity. The results are shown in Figs. 7(a) and (b). As expected, the sintered region is significantly smaller than that in Fig. 6. Like the case with slow scanning velocity plotted in Fig. 6(a), the predicted shape and size of the cross sections is almost the same for three different x.

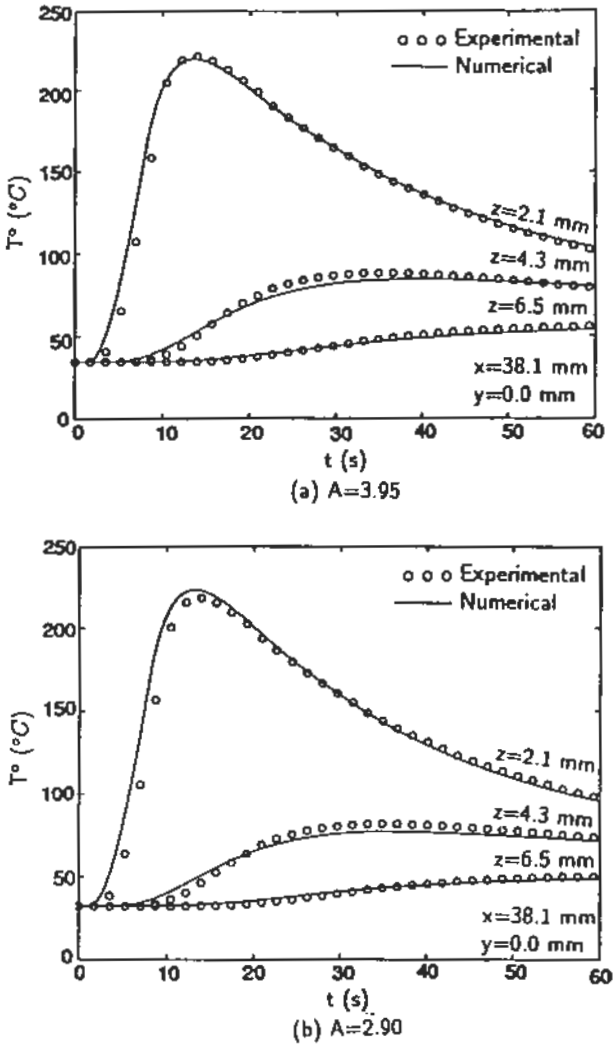

Figure 5: Comparison of temperature histories obtained by numerical simulation and experiment (stationary laser beam)

Fig. 8 shows the top and bottom of the HAZ for different scanning velocities at y=0. For the slower scanning case, the sintered depth reaches its maximum value at $x = 31mm$, which is about $3mm$ beyond the starting point of scanning, and the sintering depth remains unchanged until $x = 47mm$ ($1mm$ before the stopping point of the laser scan). For the faster scanning case, the sintering starts at a slightly larger x. The variation of the sintering depth with x is similar to that of slower scanning case. Fig. 9 (a) and (b) show the comparison of the temperature history obtained numerically and experimentally. The agreement between the numerical and experimental results is very good.

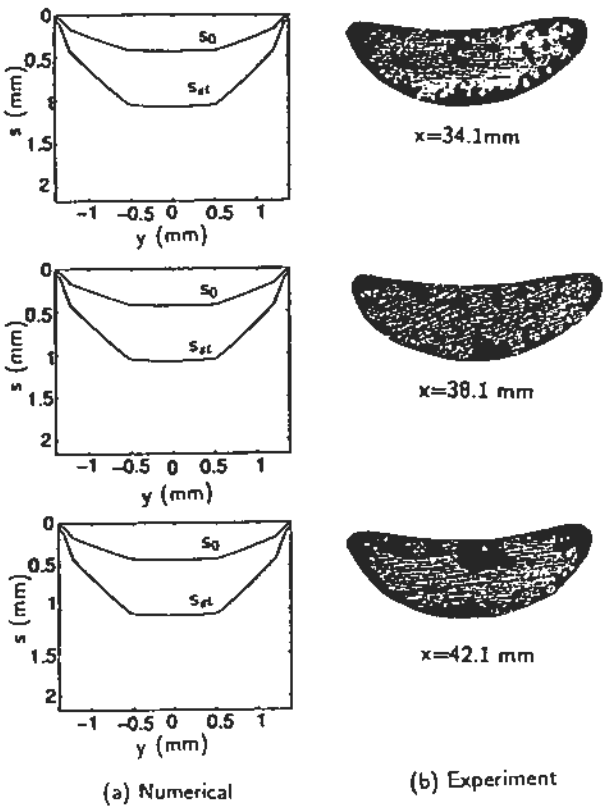

Figure 6: Comparison of the cross section area obtained by numerical simulation and experiment (moving laser beam: $A = 1.0, N_i = 0.0749, U_b = 0.124$)

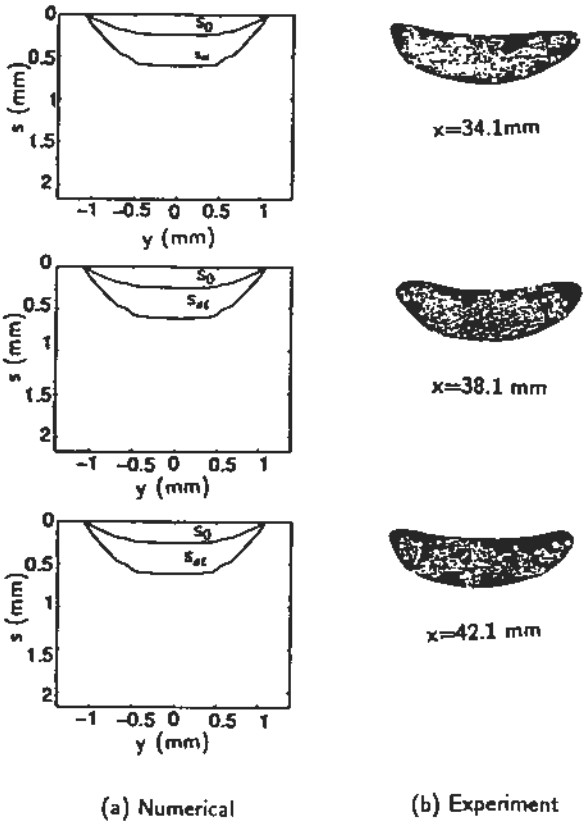

Figure 7: Comparison of the cross section area obtained by numerical simulation and experiment (moving laser beam: $A = 1.0, N_i = 0.0749, U_b = 0.248$)

The variation of dimensionless HAZ cross sectional area with the dimensionless laser intensity at two different scanning velocities is shown in Fig. 10(a). The predicted and measured dimensionless cross sectional areas were obtained by $A_c = 2\int_0^{Y_D} [\eta_{st}(X_D/2, Y) - \eta_0(X_D/2, Y)]\, dY$ and by measuring the sintered area (i.e. light area in photos such as those in Fig. 6 and 7), respectively. As can be seen, both predicted and measured A_c vary linearly with N_i. The predicted cross sectional areas are in general smaller than the measured values. Considering the uncertainty in the absorptivity and the thermal properties of both powders, as well as the uncertainty in measuring A_c, the agreement between the predicted and measured A_c is very good. Based on the experimental results in Fig. 10(a), an empirical correlation of A_c is proposed:

$$A_c = 1.79\frac{N_i}{U_b} + 0.557U_b - 0.292 \qquad (22)$$

Comparison of experimental results and eq. (22) is shown in Fig. 10(b). The difference between the measured A_c and eq. (22) is less than 15%. Of course, a different correlation would result if different materials are used.

CONCLUSION

3-D sintering of two metal powders with significantly different melting points with stationary and moving laser beam has been investigated numerically and experimentally. The shrinkage of the powder bed due to the density change and the liquid flow driven by the capillary and gravity forces were taken into account. Experiments with nickel braze as the low melting point powder and AISI 1080 steel powder as the high melting point powder were performed. The numerical simulation

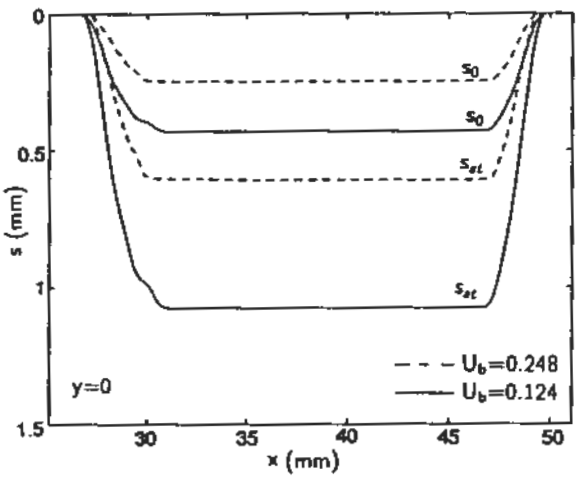

Figure 8: Effect of the scanning velocity on the cross sections at y=0 (moving laser beam: $A = 1.0, N_i = 0.0749$)

and experiment were performed for both a stationary ellipsoid laser beam and a moving round laser beam. The temperature histories obtained by the numerical simulation and the experiment agreed very well. The boundary between sintered and unsintered powder was clear for numerical results but it was not clear for the experimental results, which may be caused by a non-equilibrium state existing between the low melting point liquid metal and the solid particles at the boundary. The effects of laser properties and scanning velocity on the SLS process were also investigated. An empirical correlation of the cross section area of the HAZ was proposed.

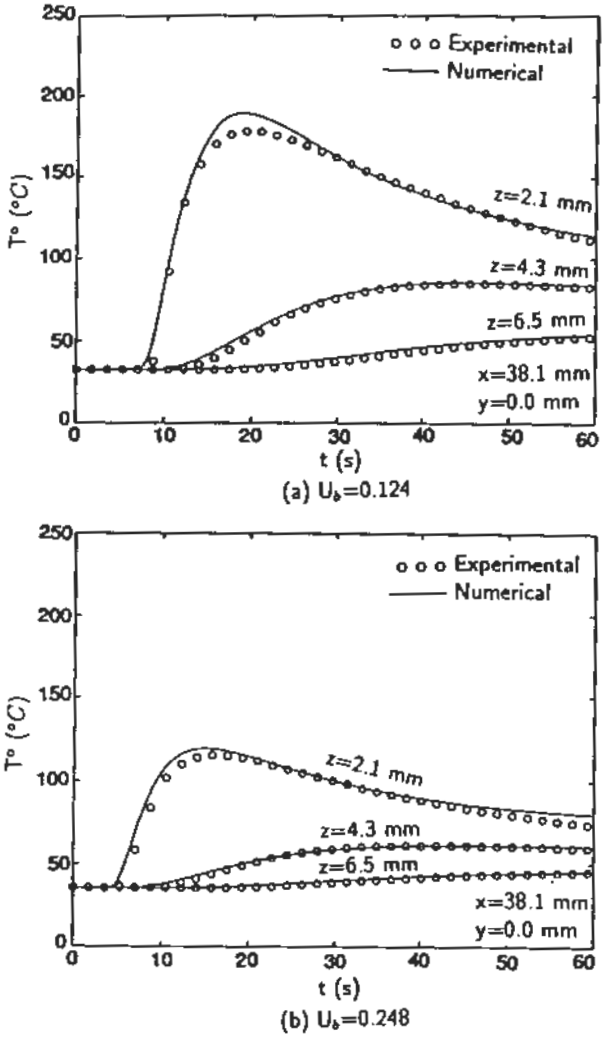

Figure 9: Comparison of temperature histories obtained by numerical simulation and experiment (moving laser beam: $A = 1.0, N_i = 0.0749$)

ACKNOWLEDGMENT

CWB and TLB acknowledge the support of the National Science Foundation under Grant No. 9796186.

REFERENCES

Beaman, J.J., Barlow, J.W., Bourell, D.L., Crawford, R.H., Marcus, H.L., and McAlea, K.P., 1997, *Solid Freeform Fabrication: A New Direction in Manufacturing*, Kluwer Academic Publishers, Bordrecht.

Brandes, E.A., 1983, *Smithells Metals Reference Book*, Butterworth & Co. Ltd., London.

Bunnell, D. E., 1995, *Fundamentals of Selective Laser Sintering of Metals*, Ph.D. Thesis, University of Texas at Austin.

Cao, Y., and Faghri, A., 1990, A Numerical Analysis of Phase Change Problems Including Natural Convection, *ASME Journal of Heat Transfer*, Vol. 112, pp. 812-816.

Hadley, G.R., 1986, Thermal Conductivity of Packed Metal Powders, *InternationalJournal Heat and Mass Transfer*, Vol. 29, pp. 909-920.

Iida, T., and Guthrie, R.I.L., 1988, *The Physical Properties of Liquid Metals*, Oxford University Press, Oxford.

Incropera, F.P., and DeWitt, D.P., 1996, *Fun-*

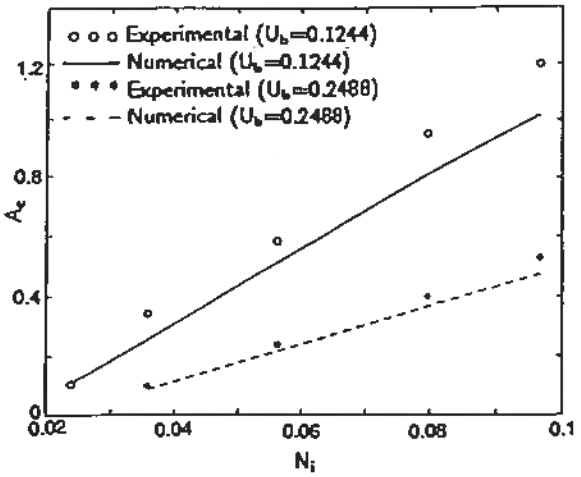

(a) Comparison of cross section area of HAZ

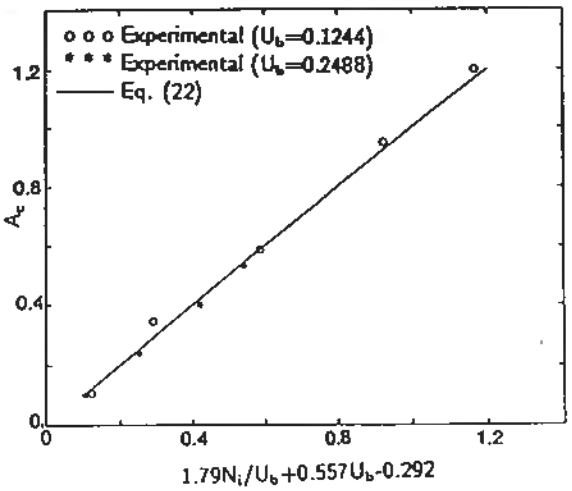

(b) Empirical correlation of cross section area of HAZ

Figure 10: Cross section area of the HAZ at different laser intensities and scanning velocities

damentals of Heat and Mass Transfer, 4th Edition, John Wiley & Sons, New York.

Kandis, M., Buckley, C.W., Bergman, T.L., 1999, An Engineering Model for Laser-Induced Sintering of Polymer Powders, *ASME Journal of Manufacturing Science and Engineering* (in press)

Kandis, M., and Bergman, T.L., 1997, Observation, Prediction, and Correlation of Geometric Shape Evolution Induced by Non-Isothermal Sintering of Polymer Powder, *ASME Journal of Heat Transfer*, Vol. 119, pp. 824-831.

Kaviany, M., 1995, *Principles of Heat Transfer in Porous Media*, 2nd Edition, Springer-Verlag, New York.

Manzur, T., DeMaria, T., Chen, W., and Roychoudhuri, C., 1996, Potential Role of High Power Laser Diode in Manufacturing, presented at SPIE Photonics West Conference, San Jose, CA.

Mughal, M., and Plumb, O.A., 1993, Thermal Densification of Metal-Ceramic Composites, *Scripta Metallurgica et Materialia*, Vol. 29, pp. 383-388.

Pak, J., and Plumb, O.A., 1997, Melting in a Two-Component Packed Bed, *ASME Journal of Heat Transfer*, Vol. 119, pp. 553-559.

Patankar, S.V., 1980, *Numerical Heat Transfer and Fluid Flow*, McGraw-Hill, New York.

Shah, A.A., 1994, Thermomechanical Compressive Melting of Solder Particles, MS Thesis, University of Texas at Austin.

Siegel, R., and Howell, J.R., 1992, *Thermal Radiation Heat Transfer*, 3rd Edition, Hemisphere, Washington, DC.

Sun, M.M., and Beaman, J.J., 1995, A Three Dimensional Model for Selective Laser Sintering, *Proceedings of Solid Freeform Fabrication Symposium 1995*, H.L. Marcus et al., eds., pp. 102-109.

Touloukian, Y.S., 1967, *Thermophysical Properties of High Temperature Solid Materials, Vol. 2: Nonferrous Alloys*, Thermophysical Properties Research Center, Purdue University, West Lafayette, IN.

Von Allmen, M., 1986, *Laser-Beam Interactions with Materials*, Springer-Verlag, New York.

Wall Colmonoy Corporation, 1997, Material Safety Data Sheet of Nickel Braze.

Williams, J., Miller, D., and Deckard, C., 1996, Selective Laser Sintering Part Strength as Function of Andrew Number, Scan Rate and Spot Size, *Proceedings of Solid Freeform Fabrication Symposium 1996*, H.L. Marcus et al., eds., pp. 549-557.

Zhang, Y., 1998, *Thermal Modeling of Advanced Manufacturing Technologies: Grinding, Laser Drilling, and Solid Freeform Fabrication*, Ph.D. Dissertation, University of Connecticut.

Zhang, Y., and Faghri, A., 1998, Melting and Resolidification of a Subcooled Mixed Powder Bed with Moving Gaussian Heat Source, *ASME Journal of Heat Transfer*, Vol. 120, No. 4, pp. 883-891.

Zhang, Y., and Faghri, A., 1999, Melting of a Subcooled Mixed Powder Bed with Constant Heat Flux Heating, *InternationalJournal Heat and Mass Transfer*, Vol. 42, pp. 775-788.